Soil profile stratigraphy detected by ground penetrating radar in the modern Yellow River Delta

Ping Wang[1], Xinju Li[2], Xiangyu Min[2] and Shuo Xu[1]

[1] School of Geography and Tourism, Qufu Normal University, Rizhao, China.

[2] College of Resources and Environment, Shandong Agricultural University, Tai'an, China.

Corresponding author: P. Wang (wpqfnu@qfnu.edu.cn)

†Corresponding author: Ping Wang

E-mail: wpqfnu@qfnu.edu.cn

Tel: (+86)18263366900

Address: School of Geography and Tourism, Qufu Normal University, Yan Tai Bei Lu 80, Rizhao, Shandong Province, China

Zip code: 276826

Key Points:

- GPR with 250MHz antennas can identify the 0-1m soil profile stratigraphy in the modern Yellow River Delta, and soil cultivation layer under different land use patterns is clearly discernible in the GPR spectrum images.
- By substituting the measured soil water content and comparing GPR spectrum images with the amplitude-time plots, the average error of the estimated soil layer thickness can reach 0.040m.
- The compound effect of soil water and salt on the GPR signals is strong, and the second derivative values of envelop amplitude energy have negative logarithmic function and power function with soil water content and electrical conductivity values, respectively.

Abstract

Soil profile stratigraphy plays a fundamental role in the vertical movement of soil water and salt, land cover and land use pattern change in the modern Yellow River Delta. We investigated 22 typical soil profiles with ground penetrating radar (GPR) of 250 MHz antenna according to the tail wing changes over the past 130 years, calculated soil dielectric permittivity and electromagnetic wave propagation velocity with measured soil water content, acquired the electromagnetic wave propagation time from the amplitude-time matrix and finally calculated the thickness of different soil layers. The results showed that GPR can identify the 0-1m soil profile stratigraphy, and soil cultivation layer under different land use patterns is clearly discernible. The comparison of GPR spectrum image and amplitude-time plot is helpful to reduce the estimation error of soil layer thickness. The average error of the estimated soil layer thickness is 0.040m and the error of 54 soil layers in total 58 soil layers is less than 0.100m. The comprehensive effect of soil physical and chemical characteristics affects the electromagnetic wave signals and the profile stratigraphy identification. The more similar the morphological characteristics of spectral images are, the closer the soil properties are. The compound effect of soil water and salt is strong, and the second derivative values of envelop amplitude energy have negative logarithmic function and power function with soil water content and electrical conductivity values, respectively. This study indicated the feasibility of using GPR to investigate coastal saline soil stratigraphy in the modern Yellow River Delta.

1. Introduction

The Yellow River Delta is a young delta plain formed by sediment deposition in the estuary of the Yellow River and up to now, the land area is growing. Due to the different physical and chemical properties of the deposition in different depositional periods, the spatial variation of

soil profile stratigraphy is remarkable. There are three basic stratigraphies: the full profile of sandy loam, the profile of clay soil sandwiched in the sand loam and the profile with clay as topsoil and sandy loam as bottom [*Zhang*, 2010]. The soil stratigraphy can fundamentally affect the vertical movement of water and salt, resulted in the variation of land cover and land use pattern [*Romero-Ruiz et al.*, 2018]. Considering the spatial heterogeneity of soil properties and land use patterns, GPR, as a tool for the mesoscale investigation, is suitable for soil survey in the Yellow River Delta [*Yao et al.*, 2006]. Compared with the traditional survey methods, such as pit digging and hole drilling, GPR can retrieve soil profile stratigraphy and identify soil layers along the survey line, which has the characteristics of short time-consuming, low labor intensity and less soil damage; compared with remote sensing observation, GPR has the advantages of high precision and deep measurement [*Jackson et al.*, 1996; *Cavallo et al.*, 2016; *Brevik et al.*, 2016; *Zajícová &Chuman*, 2019].

Based on the electromagnetic (EM) characteristics of the medium, GPR reports soil characteristics through the changes of dielectric permittivity, EM wave velocity and amplitude. GPR can identify soil layers with different dielectric permittivity, and detect the variation of soil dielectric permittivity in the same soil genetic layer [*Cavallo et al.*, 2016; *Walter et al.*, 2016; *Wang et al.*, 2016a; *Yao et al.*, 2006; *Zhang et al.*, 2014]. Relevant studies include the determination of soil weathering layer [*Aranha et al.*, 2002; *Cao et al.*, 2017], depth and spatial variability of clay deposits [*Truman et al.*, 1988], interface and depth of loess alluvial soil in different periods [*Inman et al.*, 2001], different peat layer types and the thickness of aquatic sediments [*Hnninen*, 1992; *Sass O. et al.*, 2010; *Casey D.K. et al.*, 2018]. The correlation between GPR detection and traditional measurement of soil layer depth is above 0.9. GPR with 60-900 MHz central frequency can measure soil profile stratigraphy with depth of 0.08-9m, and

considering the detection depth and vertical resolution, GPR with 200MHz central frequency is more suitable for the regional investigation of soil profile stratigraphy within 1 m [*Butnor et al.*, 2014; *Li et al.*, 2015; *Sukhobok et al.*, 2016; *Cao et al.*, 2019; *Luo et al.*, 2019]. The linear regression model combined with gene expression programming algorithm is established between GPR detection depth and weathering index of bedrock [*Wang et al.*, 2016c], and the multi-layer boundary is automatically identified by reflection coefficient and refraction angle [*Romero-Ruiz et al.*, 2018]. Lombardi & Lualdi [2019] demonstrated that the frequency dependence of EM properties of inhomogeneous soil are significant for defining the subsurface attributes.

Water content is the dominant factor affecting soil dielectric permittivity and GPR signal transmission ability. Salt dissolved in soil capillary water can cause high attenuation of GPR signal and limit the penetration depth due to its high conductivity. Doolittle et al. [2007] found the saline soil (saturated conductivity higher than 4 mS/cm) and sodium soil (sodium absorption more than 13) not suitable for the application of GPR. However, there are still many achievements in the application of GPR in the saline soil area, including the extraction of soil alkaline layer [*Maury & Balaji*, 2015; *Kumar et al.*, 2016; *Samson et al.*, 2017], the distinction of soil boundary between arable land and saline-alkaline land, the analysis of the influence of soil salinity on GPR spectrum images [*Maury & Balaji*, 2015; *Kumar et al.*, 2016], and the assessment of salinity changes in the depth direction [*Peng et al.*, 2009; *Samson et al.*, 2017]. Through the plot tests in the Yellow River Delta, it was found that GPR can distinguish soil profiles with different vegetation coverage (bare land, reed, suaeda salsa, thatch) or growth conditions (in a wheat field, some parts are bare, some parts where wheat does not grow densely, and some parts where wheat grows densely) along the survey line with the horizontal discrimination error mostly less than 0.5m; it can detect soil layers within 1 m depth with the

vertical discrimination error less than 0.1 m [*Wang et al.*, 2016b; *Wang et al.*, 2017]. Soil water, salt and clay content have a close impact on EM wave, affecting the strength of reflected signal and the picking accuracy of soil interface [*Butnor et al.*, 2014; *Samson et al.*, 2017]. Ju [2005] found that the dielectric permittivity of drying soil was negatively correlated with the content of soil organic matter, and Xue et al. [2005] quantitatively evaluate the degree of soil salinization with the correlation between high and medium frequency peak values and soil organic matter content. Most of the results of GPR quantitative research on soil salinity focus on soil pollutant transport observation and pollution degree evaluation [*Hu et al.*, 2006; *Wang et al.*, 2015]. For high salinity soil, the attenuation of high frequency component of GPR signal is higher than that of low frequency component [*Kumar et al.*, 2016]. We usually use statistical or neural network methods to construct the relationship models among soil salinity, dielectric permittivity and amplitude under different water and texture conditions [*Scudiero et al.*, 2012].

The objective of this study is to explore the feasibility and accuracy of GPR in soil profile stratigraphy survey in the whole modern Yellow River Delta. Referring to research ideas from Zhang et al. [2014], this study puts forward a simple and accurate GPR data analysis and processing idea, analyzes the influence characteristics of soil water, salt and other factors on EM wave signal, and lays the foundation for the future GPR survey of soil characteristics in this area.

2. Study area

The study area is located in the flat delta zone of the Yellow River estuary (Figure 1). Since 1855, the Yellow River was diverted to the Bohai Sea and the modern Yellow River Delta has been formed with Ninghai Town, Kenli County as its apex, north from the Tuer Estuary and south to the Zimai Estuary. Affected by the continental monsoon climate in the North Temperate Zone, the precipitation is mainly concentrated from June to August, accounting for 70% of the

annual precipitation. The groundwater depth ranges from 1.2 to 3.0 m [*Liu et al.*, 2019], and the evapotranspiration-drop ratio can reach about 3.5. The soil type is mainly saline alluvial soil with salt accumulation on the surface [*Gan et al.*, 2019].

Figure 1 showed the 11 flow paths formed on the modern Yellow River Delta, and marks the formation and abandonment time (year) of each flow path. Referring to the book "Soil and Environment of the Yellow River Delta" written by Yantai Coastal Zone Research Institute, Chinese Academy of Sciences, according to the location and stratigraphy of typical soil profiles, and the physical and chemical characteristics of each soil layer introduced in the book, we selected 22 typical soil profiles along the flow paths in different periods as the measurement spots of this study.

At each spot, we first carried out GPR survey, then excavated soil profile, and collected soil samples according to actual soil stratigraphy. The length of GPR survey lines are between 13.65 to 31.99 m, and the excavated soil profiles are located at the midpoint or adjacent area of each GPR survey line. In the field, we collected soil bulk density samples with cutting ring method and gathered soil samples into sealed bags. Considering that the compaction at the bottom makes the ring difficult to enter the soil, and high sand content makes it difficult to acquire a complete ring sample, most of the bulk density samples are at the soil layers above 60 cm. In the laboratory, soil bulk density and water content were measured with drying method, and EC value was measured by American HQ30D portable meters. Mastersizer 3000 laser diffraction particle size analyzer measured soil particle size composition, soil texture types were determined according to International Classification System, proposed by Atterberg A. in 1912 and adopted in the 2th International Soil Society in 1930. Table 1 listed soil characteristics of some spots.


Yellow River
Beijing
Study Area

(a) (b)

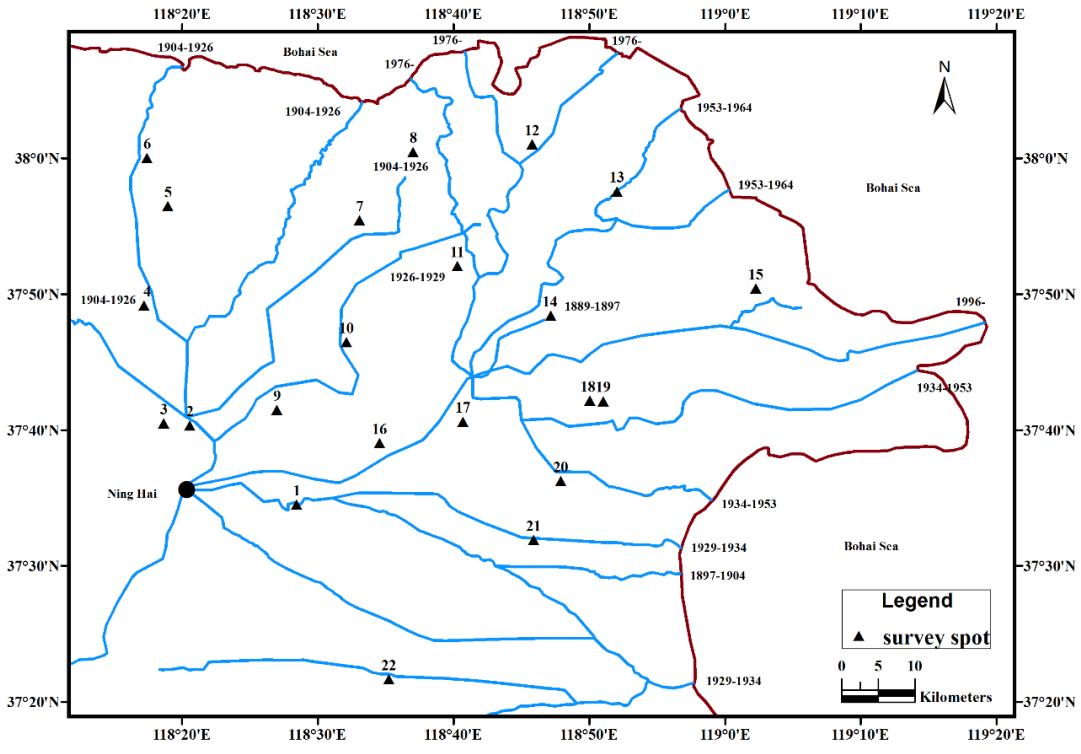
118°20'E
118°30'E
118°40'E
118°50'E
119°0'E
119°10'E
119°20'E
38°0'N
37°50'N
37°40'N
37°30'N
37°20'N
Bohai Sea
1904-1926
1976-
1953-1964
1926-1929
1889-1897
1996-
1819
1934-1953
1929-1934
1897-1904
Ning Hai
N
Legend
survey spot
0 5 10
Kilometers

(c)

(d) (e)

Figure 1. (a) The location of study area; (b) GPR measurement in rice field; (c) The flow paths of Yellow River in different periods; (d) GPR measurement in cotton field; (e) GPR measurement in reed-suaeda salsa-cotton field.

Table 1. Soil characteristics of different layers in some spots.

Spot No.	Soil type	Land use	Sampling level (m)	Bulk density (g/cm^3)	Water content (%)	EC (mS/cm)	Particle size ratio (<0.002mm) (%)	Particle size ratio (0.002-0.02mm) (%)	Particle size ratio (0.02-2mm) (%)	Soil Texture
1	Salinized alluvial soil with loam chloride	Rice	0-15	1.56	21.19	0.62	3.61	23.68	72.70	Sandy loam
			15-30	-	17.96	0.24	2.91	23.90	73.18	Sandy loam
			30-45	-	18.82	0.26	2.13	18.50	79.37	Sandy loam
			>45	-	22.24	0.26	2.60	22.04	75.36	Sandy loam
6	Loamy coastal saline soil	Reed, Suaeda salsa and cotton	0-20	1.47	15.60	0.73	4.33	48.78	46.88	Silty loam
			20-40	1.39	21.73	1.10	9.52	55.32	35.17	Silty loam
			40-80		18.55	1.58	3.90	41.37	54.75	Loam

			>80		19.41	1.47	4.44	44.71	50.84	Loam
7	Loamy coastal saline soil	Reed	0-15	1.45	19.21	0.94	6.57	49.74	43.69	Silty loam
			15-30	1.46	18.87	1.14	4.72	49.23	46.05	Silty loam
			>30		29.95	1.80	5.68	54.17	40.14	Silty loam
8	Salinized alluvial soil with loam chloride	Reed and Suaeda salsa	0-10	1.63	17.50	13.85	4.00	48.78	47.21	Silty loam
			10-20	1.45	24.29	7.54	5.64	67.95	26.40	Silty loam
			20-40	1.61	19.83	3.80	2.13	12.17	85.70	Loamy sandy soil
			>40	1.62	19.97	2.59	1.88	12.96	85.16	Loamy sandy soil
9	Salinized alluvial soil with loam chloride	Cotton	0-15	1.59	19.44	0.70	5.28	58.52	36.20	Silty loam
			15-45	1.54	18.59	0.63	2.78	25.00	72.22	Sandy loam
			45-70	-	21.96	0.60	3.29	40.31	56.40	Sandy loam
			>70	-	19.46	0.33	4.35	33.68	61.98	Sandy loam
11	Grey clayey alluvial soil	Wheat	0-30	1.42	13.92	0.12	3.71	29.07	67.22	Sandy loam
			30-60	1.43	11.95	0.14	2.53	22.18	75.29	Sandy loam
			>60	-	24.91	0.53	6.55	63.90	29.55	Silty loam
12	Clay chloride saline alluvial soil	Reed and Suaeda salsa	0-30	1.63	18.15	3.33	1.66	8.61	89.74	Loamy sandy soil
			30-60	-	18.97	3.22	1.62	5.40	92.98	Loamy sandy soil
			>60	-	18.09	3.00	1.49	6.47	92.05	Loamy

										sandy soil
15	Lime-sand alluvial soil	Reed and Tamarix chinensis	0-40	1.65	14.80	11.43	3.19	32.62	64.19	Sandy loam
			40-60	1.61	19.01	4.18	3.10	37.90	58.99	Sandy loam
			>60	-	19.82	2.67	3.63	44.35	52.01	Loam
17	Salinized alluvial soil with loam chloride	Cotton and Suaeda salsa	0-30	1.45	14.27	1.17	4.78	46.66	48.55	Silty loam
			30-60	1.52	13.94	1.30	4.50	47.52	47.99	Silty loam
			60-80	-	20.78	1.95	3.51	37.39	59.12	Sandy loam
			>80	-	31.25	3.32	4.47	33.91	61.61	Sandy loam
19	Salinized alluvial soil with loam chloride	Cotton	0-30	1.59	14.89	2.41	3.73	37.05	59.22	Sandy loam
			30-45	1.39	14.23	2.13	2.60	21.71	75.69	Sandy loam
			45-60		22.44	2.91	4.34	54.67	40.98	Silty loam
			>60		11.87	1.50	2.13	15.79	82.07	Sandy loam
20	Loamy coastal saline soil	Cotton	0-30	1.55	17.57	0.10	2.84	24.89	72.28	Sandy loam
			30-60	1.56	20.37	0.11	2.34	9.32	88.34	Loamy sandy soil
			>60		19.95	0.15	1.99	10.33	87.67	Loamy sandy soil
21	Loamy coastal saline soil	Cotton	0-20	1.62	9.43	0.14	4.37	36.83	58.80	Sandy loam
			20-60	1.41	14.61	0.58	5.02	49.52	45.46	Silty loam
			>60	-	19.44	1.19	3.37	38.81	57.82	Sandy loam

			0-30	1.19	11.44	0.72	4.80	48.67	46.52	Silty loam
22	Loamy coastal saline soil	Wheat	30-60	1.64	15.70	0.70	4.89	48.88	46.23	Silty loam
			>60		21.44	1.27	4.50	61.79	33.71	Silty loam

3. Data and Methods

3.1. GPR equipment

The higher the frequency of GPR antenna is, the shallower the detection depth is [*Butnor et al.*, 2014; *Li et al.*, 2015; *Cao et al.*, 2019]. In addition, soil water and salt promote the rapid attenuation of high-frequency EM wave, so we employed pulseEKKO PRO GPR with the central frequency of 250 MHz. The relationship between the vertical resolution Z and radar wave length λ [*Widess*, 2001] is proposed to be:

$$Z = \left(\frac{1}{8} \sim \frac{1}{4}\right)\lambda = \left(\frac{1}{8} \sim \frac{1}{4}\right)\frac{v}{f} \quad (1)$$

Where, v and f represents the propagation velocity and EM wave frequency, respectively. In the survey, the propagation velocity is between 0.071 and 0.132 m/ns, so the vertical resolution is about 3.55-13.20 cm for GPR with 250 MHz antenna. We used fixed offset data collection method with the antennas' internal spacing of 0.38 m, set the time window of 48 ns, the spatial sampling interval of 0.04 m and the detection depth of about 2 m (the preset velocity is 0.1 m/ns). At each spot, GPR survey was repeated three times, and the best measurement result is selected for data analysis.

3.2. EM wave signal processing

The initial processing of EM wave signal consists of five steps: zero-time adjusting, background subtraction, band pass filter, the Automatic Gain Control (AGC) gain and horizontal average

filter. Zero-time adjusting aims at obtaining the accurate starting time of EM wave. Background subtraction is used to apply a running-average background subtraction to the data set and remove localized flat-lying events. There is significant difference in radar spectral images before and after background subtraction (Figure 2a). However, I don't like to use the background subtraction method to identify the sedimentary stratigraphy because this step is not conducive to reading the smooth soil layer, but will highlight the influence of cultivation, crop roots, large stone and soil pores. The purpose of band pass filter is to enhance the desired signals at the expense of the out-of-band noise. With Spot 11 as a reference, when soil water content increases (e.g., Spot 20, Table 1), or when soil salt content increases (e.g., Spot 15, Table 1), GPR signals change significantly in the frequency domain greater than 300 MHz (Figure 2c). Hu et al. [2006] also found that the increase of salt mainly led to some secondary peaks in the high-frequency region. However, the band-pass filter (retaining 70-300MHz) has little effect on the GPR spectral image (Figure 2b). AGC gain applies a gain which is inversely proportional to the signal strength and is helpful for defining continuity of reflecting events. Horizontal average filter applies a running average filter along the GPR detection line to emphasize flat-lying reflectors.

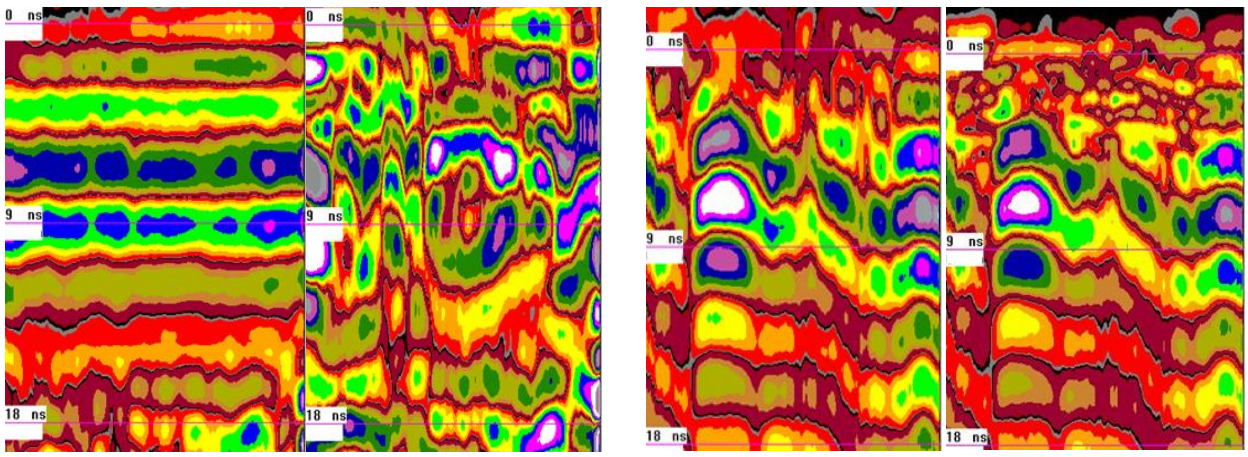

(a) (b)

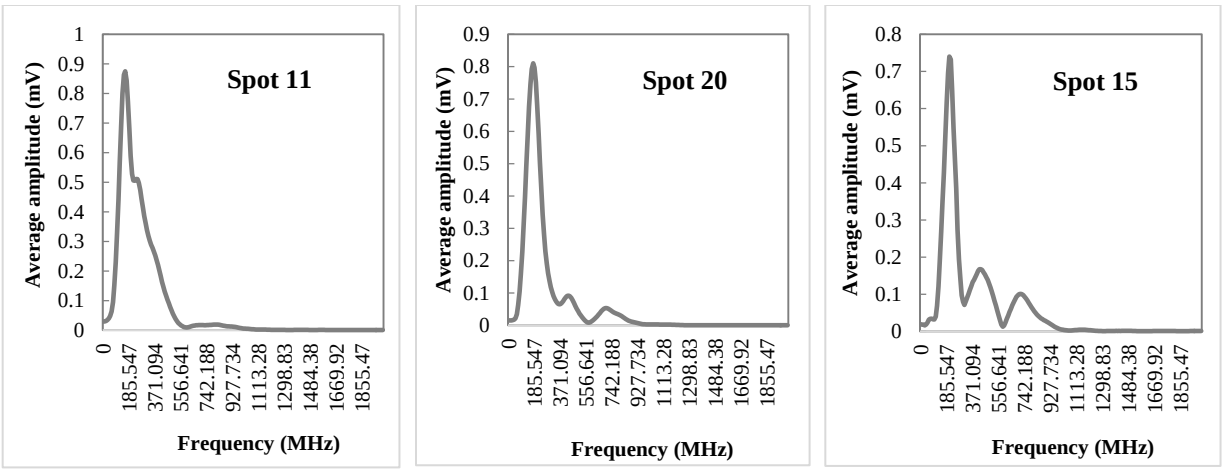

(c)

Figure 2. (a) Contrast maps before and after background subtraction of Spot 1 (Left: before background subtraction, Right: after background subtraction); (b) Contrast maps before and after band-pass filtering of Spot 17 (Left: before band-pass filtering, Right: after band-pass filtering); (c) The amplitude-frequency maps of Spot 11, 20 and 15.

Considering the continuity of soil layer, upholding the principle of using the most simplified steps and obtaining the clearest radargrams, the data processing was simplified into three steps: filtering, zero-time adjusting and gaining. On LineView software, the basic Dewow filtering process aims at eliminating unnecessary low-frequency signals and retaining high-frequency signals. The adjustment of zero time is to obtain the accurate starting time of EM wave. We use AGC method or the spreading exponential calibrated compensation (SEC) gain method to clearly reflect the difference of radargrams between different soil layers. AGC gain applies a gain function that is inversely proportional to the signal strength, with two input parameters of window width and maximum gain (Table 2). The default value of window width is 1.5 and the typical value of the maximum gain would be 50-2000 depending on the noise and average signal levels. SEC gain attempts to boost weak signals by compensating for spherical spreading losses

and exponential ohmic dissipation of energy, with three input parameters of start gain, attenuation and maximum gain (Table 2).

$$\text{SEC gain} = \text{start gain} \times \text{exponential} \quad (2)$$

Table 2. The parameters of two gain methods in the EM wave processing.

Spot No.	Gain Method				
	AGC		SEC		
	Window Width	Maximum Gain	Attenuation (dB/m)	Start Gain	Maximum Gain
1,2,13	-	-	20	8	200
3,4	1.5	500	-	-	-
5	-	-	1	5.57	236
6,9,19,20	1.5	200	-	-	-
7	1.5	50	-	-	-
8	-	-	3.23	19.01	99
10,11	-	-	20	5	500
12	-	-	5.09	12.17	125
14,22	-	-	50	8	500
15	-	-	0.5	1.5	500
16	-	-	66.06	5.19	526
17	-	-	9.84	5.33	209
18	-	-	5.33	12.47	85
21	-	-	29.93	3.72	425

The extraction of the amplitude-time information is divided into three steps: firstly, to acquire the amplitude-time matrix through LineView software, in which the amplitude values were original without gaining and other processing; secondly, to calculate the average value of amplitude at each time node; thirdly, to draw the average amplitude-time plot on Excel 2016.

3.3. The identification of soil profile stratigraphy

The selection of 0cm-depth point and soil layer interfaces directly affects the error of the identification of soil profile stratigraphy.

In the zero-time adjusting step, we obtain the exact starting time of EM wave (the first large deflection) and take it as 0ns-time point. Many times 0ns-time point doesn't indicate the arrival of the direct air wave to the receiver. We should look for 0cm-depth point manually. The antenna spacing is 0.38 meters. Assuming that the propagation velocity of air wave is 0.3 m/ns, the arrival time of air wave is about 1.2-1.3 ns. 0cm-depth point is usually chosen at the position where the amplitude waveform shows the first obvious positive reflection. The corresponding time of 0cm-depth point may be earlier or later than the arrival time of air wave. If the corresponding time of 0cm-depth point is earlier than the arrival time of the air wave, it indicates that GPR is very close to the ground. If GPR leaves the ground due to more ground cover or other reasons, there will be errors in determining 0cm-depth point.

The determination of soil layer interface on GPR spectrum may be affected by air wave, ground wave and other factors. Assuming that the propagation velocity of ground wave is 0.1 m/ns, the arrival time of ground wave is about 3.8 ns. Only depending on the color, width and spacing of spectral lines, the error of soil layer identification is large. We will comprehensively consider the influence of water and other factors on EM wave reflection signal and the positive and negative changes of reflection coefficients, compare the spectral image and amplitude-time plot, finally confirm the time node of soil interfaces, and then extract the two-way travel time of reflection waves from the amplitude-time data matrix.

In this study, the identification of soil layer stratigraphy mainly includes five steps: ① Substitute the measured water content (Table 1) into Formula (3) and (4) and obtain soil dielectric permittivity of each layer. ② Substitute soil dielectric permittivity into Formula (5) and calculate the reflection coefficient at the interface of soil layers. ③ Referring to the reflecting coefficients, compare the spectral image and amplitude-time plot of soil profile, confirm the time node of soil interfaces, and then extract the two-way travel time of reflection waves from the amplitude-time data matrix. ④ Calculate the propagation velocity of EM wave in each soil layer with Formula (6). ⑤ Substitute the results of ③ and ④ into Formula (7), and acquire the thickness of each soil layer estimated by GPR.

3.3.1. Soil dielectric permittivity

Topp model is suitable for the soil with high sand content [*Topp et al.*, 1980]. The average value of soil sand content in this study is 60.91% (see the data of some spots in Table 1), so Topp model is selected as one of the soil dielectric permittivity models. It is considered that soil dielectric permittivity (ε) is almost independent of soil texture and bulk density, and can be directly estimated by soil volumetric water content (θ):

$$\varepsilon = 3.03 + 9.3\theta + 146.0\theta^2 - 76.7\theta^3 \quad (3)$$

Ju [2005] tested 12 types of soil in different regions of China with Tectronix 1502C, and established a model between soil dielectric permittivity and volumetric water content:

$$\varepsilon = \left(\frac{\theta + 0.1846}{0.1219}\right)^2 \quad (4)$$

3.3.2. The reflection coefficient

The reflection strength of EM wave at the interface is determined by the dielectric permittivity of the two layers. The greater the difference of dielectric permittivity between the two layers, the stronger the reflection at the interface, and the easier it is to identify soil layers on radar images. According to Formula (5), the reflection coefficient can be positive or negative [*Loulizi*, 2002].

$$R(n) = \frac{\sqrt{\varepsilon_{n+1}} - \sqrt{\varepsilon_n}}{\sqrt{\varepsilon_n} + \sqrt{\varepsilon_{n+1}}} \quad (5)$$

Where, R(n) represents the reflection coefficient of EM wave at the interface between layer n and layer (n+1), ε_n and ε_{n+1} are the dielectric permittivity of the n layer and the (n+1) layer, respectively. The relative dielectric permittivity of air is assumed to be 1.

3.3.3. The propagation velocity of EM wave

For low loss soil with electrical conductivity value less than 10 mS/m [*Davis & Annan*, 1989], the propagation velocity of EM wave in each soil layer can be related to the dielectric permittivity by:

$$v = \frac{c}{\sqrt{\varepsilon}} \quad (6)$$

Where c is the velocity of EM wave in free space (0.3 m/ns).

3.3.4. The thickness of soil layer

The thickness of host soil layer (d) can be estimated by:

$$d = \frac{vt}{2} \quad (7)$$

Where t is the two-way travel time of radar signal (ns) between two soil layers. By observing the brightness, shape and spacing width of the reflected signal in the image (Figure 4 right), and comparing with the peak and trough positions in the amplitude-time plot (Figure 4 middle), we determine the position of soil layer interface and extract the two-way travel time from the amplitude-time data matrix.

3.4. The statistical correlation analysis

We use statistical methods to analyze the relationship between soil physical and chemical factors and EM wave signal. All the statistical correlation analysis work is done on SPSS software. The contents of statistical correlation analysis include: calculating Pearson correlation coefficient to describe the correlation between soil water content and EC value, using two related sample tests of nonparametric test and calculating partial correlation coefficients to analyze the correlation between envelope amplitude energy value and soil factors.

4. Results

4.1. Soil layer identification and validation

Figure 3 shows the results of five-step and three-step processing for spectral image of Spot 1. In the left picture, the spectral color changes are more abundant, and the color differences between layers within 15 ns are as follows: dark green → bright green + blue → dark green + red → yellow + red, etc. Figure 4 shows the photos of soil profiles, the processed spectral images with the estimated depth, and the amplitude-time plots with the two-way travel time of Spot 1, 11 and 17. In Spot 1, the soil of 0-15cm layer is wet, the rice roots are dense, and the humus content is high; the soil layer of 15-30 cm is a transition layer, the rice roots become less, the humus content decreases, and the soil color is light gray; the 30-45 cm soil layer is sandwiched with thin (about 1 cm thick) and discontinuous clay layer, and the clay color is reddish. However, it is not

found that the clay content is high in the 30-45 cm soil layer in Table 1, which may be related to the uneven sampling during the test. The soil layer below 45 cm is obviously wet without thin clay layer. Considering few crop roots and the strong attenuation of radar signals in the deep soil, the soil layers were not further delineated after more than 15 ns. GPR cannot touch the ground closely because of the straw stubble, so we adjusted the 0cm-depth point to 0.88 ns. In Figure 4, the differences in the shape characteristics of amplitude variation, the width and brightness of the reflection signal can be distinguished in each soil layer. According to Formula 3, 4 and 5, when the water content of the lower layer is higher than that of the upper layer, the dielectric permittivity of the lower layer is greater than that of the upper layer, and the soil reflection coefficient at the interface is positive; otherwise, the soil reflection coefficient is negative. Considering the variation of reflection coefficients (Table 3), we confirmed 3.58 ns, 8.88 ns and 11.28 ns as the boundary of soil layers, which were consistent with the color and shape changes of the left spectral image in Figure 3. The estimation error of 15-30cm soil layer is large, the main reason may be that this layer is a transition layer, and there is a certain error in the field recognition of soil layer.

In Spot 11, the main difference between 0-30cm and 30-60cm soil layers is that the former contains a large number of wheat roots, and the recognition of soil layers below 60cm is mainly based on the sudden increase of water and salt content. The 0cm-depth point was set at -0.854 ns and reflection interfaces between soil layers occurred at 5.596 ns and 10.896 ns. In Spot 17, the soil layers of 0-30cm and 30-60cm were distinguished mainly according to the changes of plant roots and soil salt content, and the soil layers below 60cm was distinguished according to the difference of soil water and salt content, in which the soil layer of 60-80cm was mixed with clay layer similar to Spot 1. The 0cm-depth point was set at 1.6265 ns and the reflection interfaces

312 between soil layers occurred at 6.6265 ns, 11.3265ns and 17.2265 ns. The estimation error of 60-
313 80cm soil layer is large, which may be due to the fact that the color difference of soil layers
314 below 30cm is not obvious, resulting in the error of soil layer recognition in the field.

315 **Table 3.** The parameters of soil layer identification for Spot 1, 11 and 17.

Spot No.	Layer thickness in the field(m)	ε		R		v (m/ns)		Layer thickness by GPR (m)		Thickness error (m)	
		Topp	Ju	Topp	Ju	Topp	Ju	Topp	Ju	Topp	Ju
1	0-15	10.828	10.581	0.534	0.530	0.091	0.092	0.123	0.125	0.027	0.025
	15-30	8.966	8.927	-0.047	-0.042	0.100	0.100	0.265	0.266	0.115	0.116
	30-45	9.440	9.353	0.013	0.012	0.098	0.098	0.117	0.118	0.033	0.032
	>45	11.477	11.149	0.049	0.044	0.089	0.090	-	-	-	-
11	0-30	6.947	7.056	0.450	0.453	0.114	0.113	0.367	0.364	0.067	0.064
	30-60	6.097	6.225	-0.033	-0.031	0.121	0.120	0.322	0.319	0.022	0.019
	>60	13.224	12.661	0.191	0.176	0.082	0.084	-	-	-	-
17	0-30	7.108	7.209	0.454	0.457	0.113	0.112	0.281	0.279	0.019	0.021
	30-60	6.954	7.063	-0.005	-0.005	0.114	0.113	0.267	0.265	0.033	0.035
	60-80	10.581	10.364	0.105	0.096	0.092	0.093	0.272	0.275	0.108	0.107
	>80	17.856	16.632	0.130	0.118	0.071	0.074	-	-	-	-

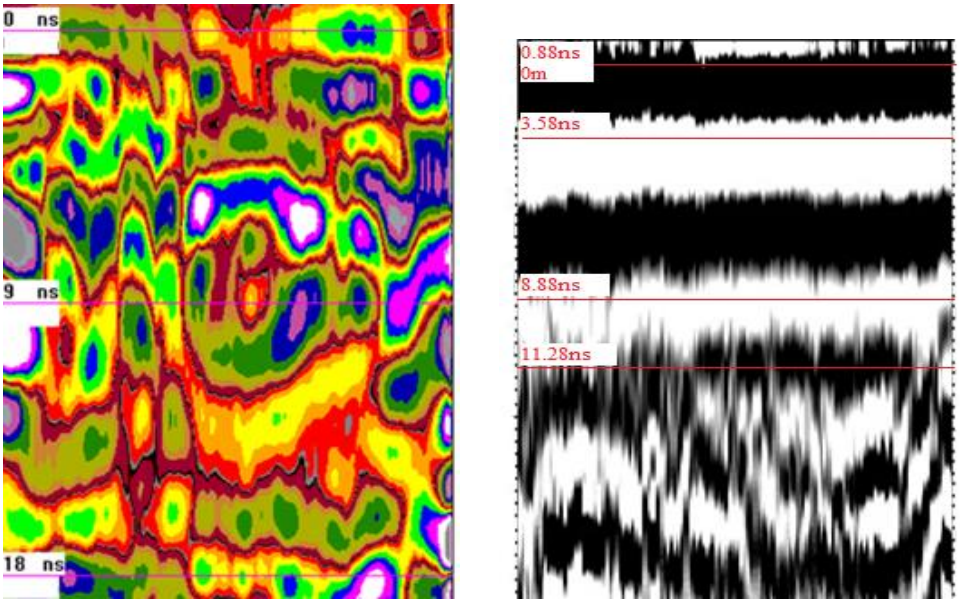

316

317 **Figure 3.** GPR images of Spot 1 (Left: the processed image with 5 steps; Right: the processed

318 image with 3 steps)

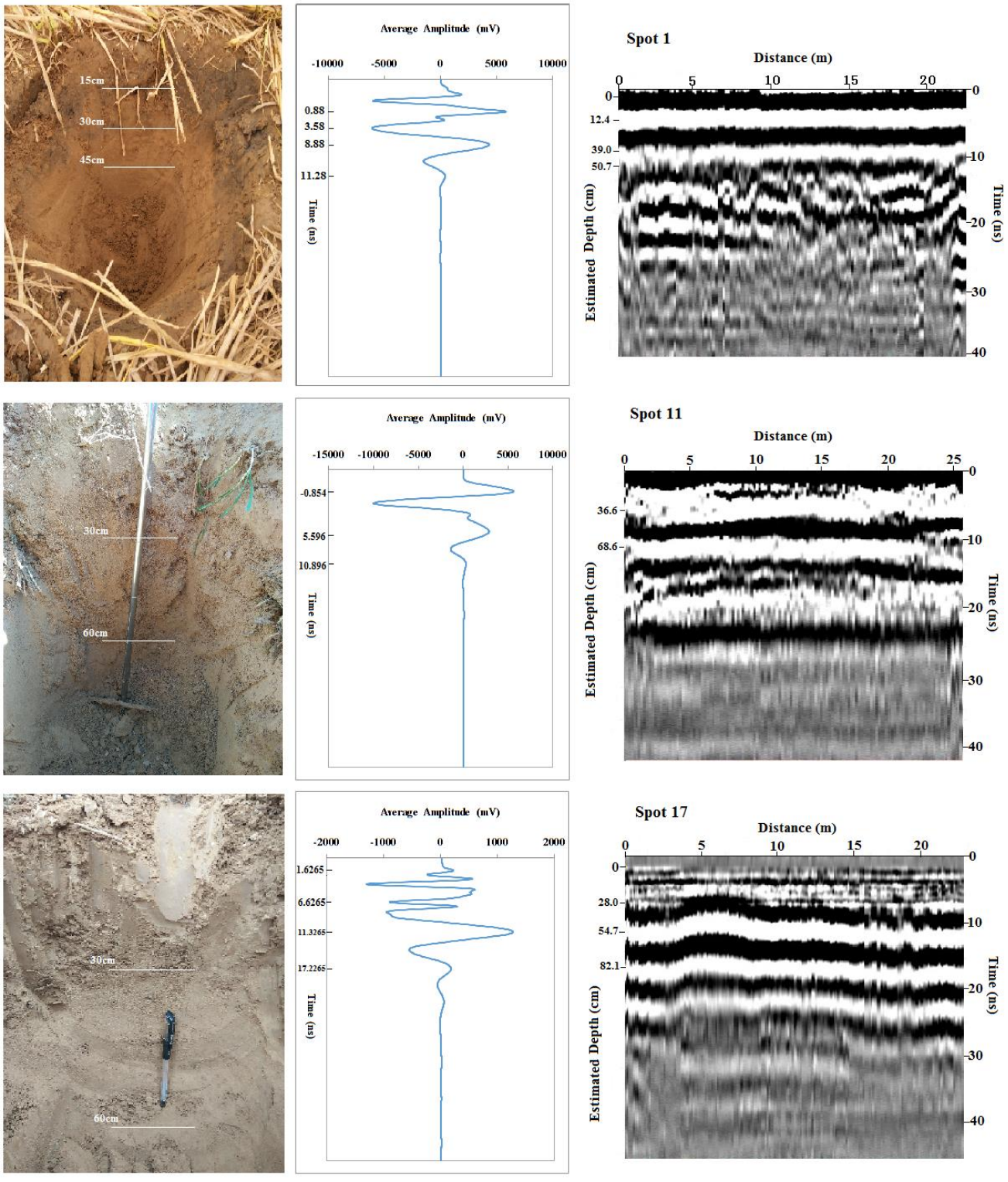
15cm
30cm
45cm
Average Amplitude (mV)
-10000
-5000
0
5000
10000
0.88
3.58
8.88
11.28
Time (ns)
Spot 1
Distance (m)
0
5
10
15
20
12.4
39.0
50.7
Estimated Depth (cm)
Time (ns)
30cm
60cm
Average Amplitude (mV)
-15000
-10000
-5000
0
5000
10000
-0.854
5.596
10.896
Time (ns)
Spot 11
Distance (m)
0
5
10
15
20
25
36.6
68.6
Estimated Depth (cm)
Time (ns)
30cm
60cm
Average Amplitude (mV)
-2000
-1000
0
1000
2000
1.6265
6.6265
11.3265
17.2265
Time (ns)
Spot 17
Distance (m)
0
5
10
15
20
28.0
54.7
82.1
Estimated Depth (cm)
Time (ns)

319

Figure 4. Layer identification of Spot 1, 11 and 17. (Left: the photos of soil profiles; Middle: the amplitude-time plots with the two-way travel time; Right: GPR images with 3 steps, in which the estimated depth is the average value of the results estimated with Topp model and Ju model.)

4.2. Soil profile stratigraphy formed in the same period

Assuming that the soil profiles formed by river sediment deposition are located close to the sea mouth in the same period, the layered characteristics of soil profiles should be similar. In this study, three groups of soil profiles, Spot 6 and 8, Spot 21 and 22, and Spot 19 and 20 were selected to analyze the differences in GPR signal characteristics of 0-1m soil profile with the same generation age and the possible reasons for the differences (Figure 5). By observing the brightness, shape and spacing width of the reflected signals, the images of Spot 19 and 20 are the most similar, followed by Spot 6 and 8, and the images of Spot 21 and 22 are quite different.

The results showed that the spectral images of soil profiles were similar under the same land use patterns, such as Spot 6 and 8, Spot 19 and 20. For Spot 21 and 22, different agricultural cultivation and soil management methods, different root types and root distribution will lead to differences in soil profile characteristics and spectral images. At about 10ns and 25ns in the middle of the survey line of Spot 21, two strong hyperbolic reflection arcs can be clearly seen, which represent the drainage pipelines.

Although the layered characteristics and the GPR spectrum images of the two soil profiles are similar, due to the physical and chemical characteristics of layered soil, the propagation velocity and amplitude of EM wave will be different. Because the water content and salt content of each soil layer are less than that of Spot 8, the EM wave propagation velocity of Spot 6 is faster, which can be seen from the corresponding depth of 10ns; the EM signal of Spot 6 attenuates

342 slowly and the propagation depth is large, in contrast, the image of Spot 8 below 20ns is not
343 clear. The soil water content, texture and bulk density of Spot 19 and 20 were similar, but the salt
344 content of Spot 19 was higher than that of Spot 20. Due to the weakening effect of salt on EM
345 wave energy, we can clearly find that the reflection band of Spot 20 is wider (stronger) than that
346 of Spot 19.

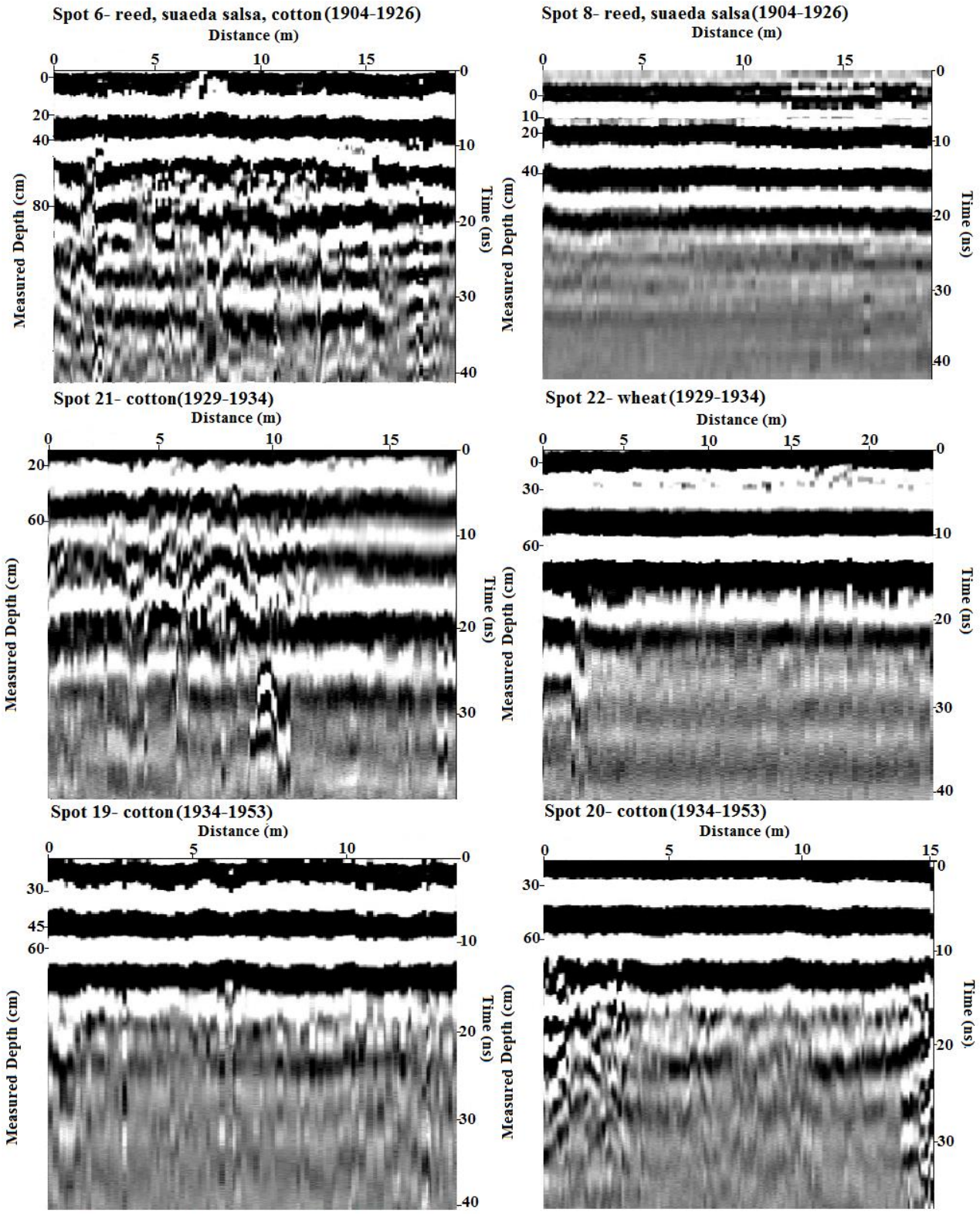

Figure 5. Three groups of soil stratigraphy formed in the same period.

4.3. Soil profile stratigraphy under typical land use patterns

As we know from Chapter 4.2, soil profile stratigraphy is closely related to land use pattern. In this study, six typical land use patterns/land cover reflecting the difference of surface soil salinization in the Yellow River Delta were selected to analyze the identification of soil profile stratigraphy by GPR (Figure 6).

4.3.1. The cultivation layer can be identified in the GPR spectrum images.

The thickness of cultivation layer is related to crop type. In GPR spectrum image, the reflected wave shape of cultivation layer is different from that of subsoil, which can show the characteristics of artificial disturbance. The thickness of cultivation layer in Spot 1 is about 30 cm, and the plough bottom is clear with the boundary between the cultivation layer and subsoil at 8.88 ns. The thickness of cultivation layer in Spot 11 is about 60 cm with the boundary at 10.896 ns, which is caused by deep ploughing in the wheat field to prevent soil hardening. The thickness of cultivation layer in Spot 17 is shallow and about 30 cm with the boundary at 6.6265 ns. Both Spot 9 and Spot 17 are planted with cotton, but because Spot 17 is a new wasteland development plot, the cultivation layer of Spot 17 seems to be more obvious than that of Spot 9.

4.3.2. The traces of the improvement and utilization of saline-alkali land can be discovered in the GPR spectrum.

Long term tillage can change the content and distribution of salt in the soil profile, and the change of cultivation layer in the GPR spectrum is an important trace. Due to the high salt content of surface soil (Table 1), the suaeda salsa land is often developed into cotton land in the process of local land improvement. Comparing the spectrum images of Spot 12 and 17, a shallow artificial cultivation layer was formed in Spot 17. Compared with the spectrum images of Spot 1 and 7, the spectral images below 45cm are similar. The reed-covered wasteland (i.e. Spot 7) is

often reclaimed as paddy field or wheat field (i.e. Spot 1 or 11) in the process of local land improvement.

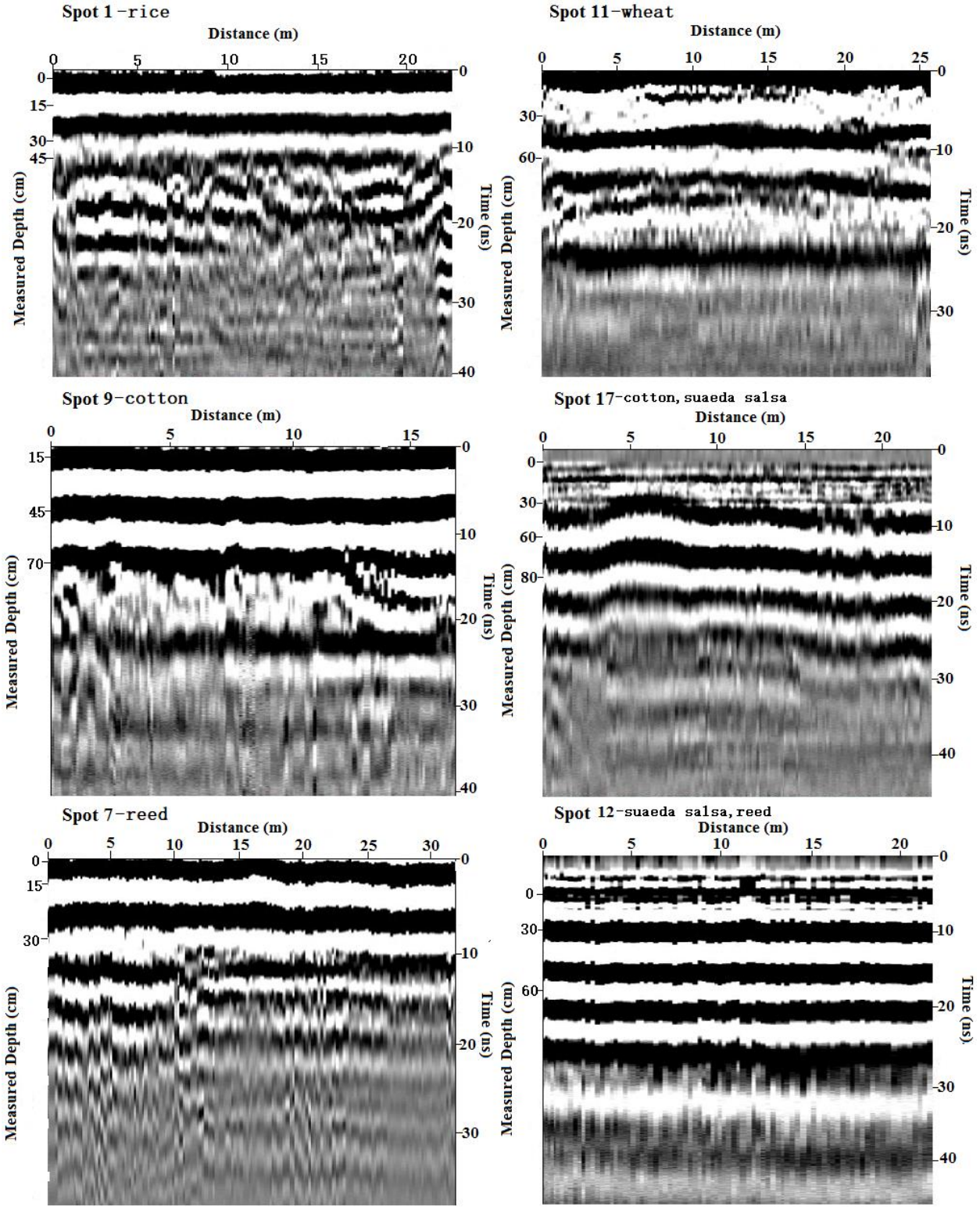

Figure 6. Six soil stratigraphies under different land use patterns.

4.3.3. The similar morphological characteristics of spectral images indicate that soil properties are similar , and vice versa.

In the 0-70cm profile of Spot 12, we can see that GPR spectrum image changes uniformly, with the similar width, brightness and spacing of reflection channels, which indicates that soil characteristics of the profile are similar (Table 1). The same phenomenon also appeared in the 0-30cm section of Spot 7 and 0-70cm section of Spot 9.

4.4. The compound influence of soil water and salt on GPR signal

It can be seen from Chapter 4.2 and 4.3.3 that GPR images of soil profile stratigraphy are related to soil physical and chemical characteristics. Soil water has the most significant effect on soil dielectric properties, affects the difference of reflection coefficient between soil layers and the recognition ability of GPR. The modified Dobson dielectric permittivity model [*Dobson et al.*,1985] shows that soil dielectric permittivity is a complex number, with the real part and imaginary part negatively correlated with soil water and salt content, respectively [*Lei et al.*, 2013]. The differences of soil bulk density, particle composition and other soil characteristics directly or indirectly affect soil water content and salt content, which lead to different responses of GPR signals .

"Salt comes with water, salt goes with water", when soil water content is high, salt content is generally high in the coastal saline area [*Zhang*, 2010]. 58 soil layers were extracted from 22 spots for analysis, and a significant positive correlation exists between soil water and salt content, with P value of 0.001 and the Spearman correlation coefficient of 0.419. The higher the soil water content, the greater the soil dielectric permittivity, the weaker EM signals and the lower the propagation velocity of EM waves. The salt dissolved in soil water also accelerates the

attenuation of EM wave signal. Under the compound influence of soil water and salt, the propagation velocity slows down and the amplitude energy decrease obviously. For Spot 15 and 21, the water and salt content of Spot 15 is higher than that of Spot 21, and the surface soil of Spot 15 has serious salt accumulation (Table 1). In the section of 0-60 cm, the amplitude energy of EM wave at Spot 15 varies between -4848.96 mV and 4218.28 mV and the average propagation velocity is 0.104 m/ns (Topp model), while the amplitude energy at Spot 21 varies between -8040.90 mV and 4427.30 mV and the average propagation velocity is 0.122 m/ns (Topp model) (Figure 7).

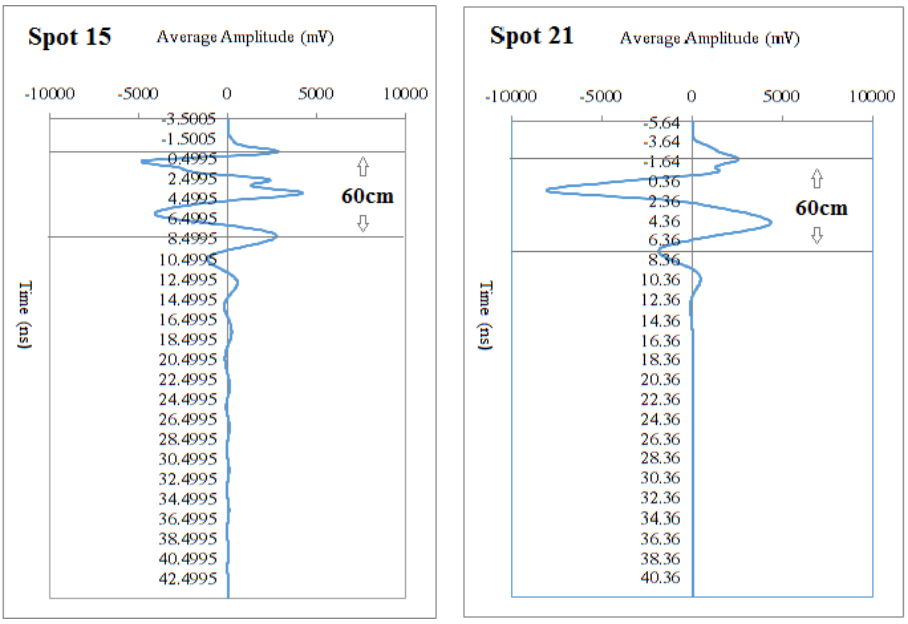

Figure 7. The amplitude-time plots of Spot 15 and 21.

5. Discussions

5.1. Error analysis of soil layer thickness estimation

5.1.1. Correlation analysis of the results of Topp model and Ju model

If there is a strong correlation between the results of Topp model and Ju model, the reliability of this study would be high. Figure 8 shows the correlation between the two sets of results,

including soil dielectric permittivity, reflection coefficient, propagation velocity of EM wave in each soil layer, and the estimated thickness of soil layer. The results of the two sets of data are similar and the correlation is very strong with correlation coefficient as high as 0.999. Overall, the soil permittivity, EM wave propagation velocity and soil thickness calculated by Ju model are slightly lower than those calculated by Topp model, while the reflection coefficient is slightly higher than that of Topp model.

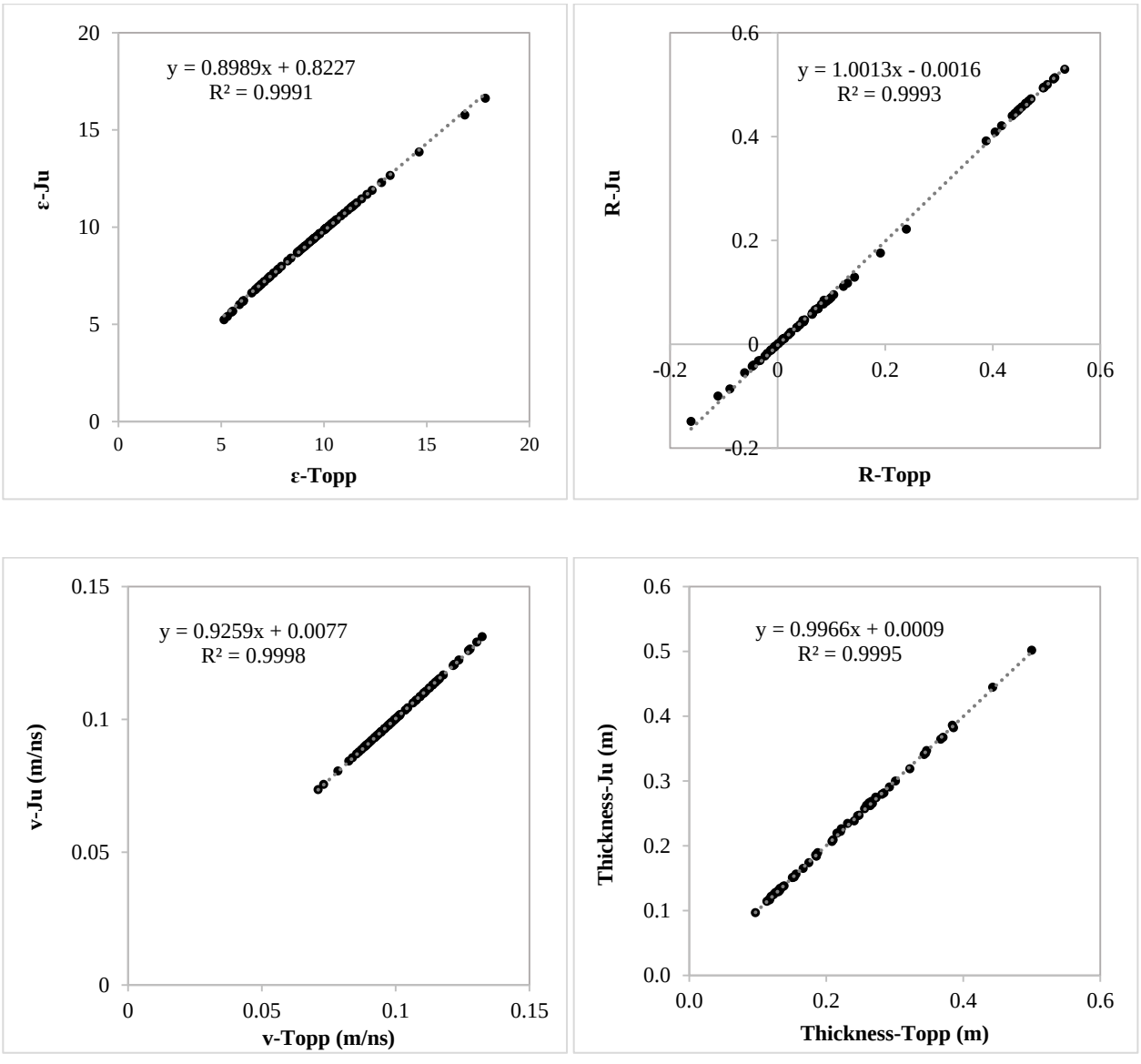

Figure 8. Correlation between calculation results of Topp model and Ju model.

5.1.2. Reasons for the increase of estimation error of soil layer thickness

(1) One of the reasons for the increase of soil thickness estimation error occurs in the step of soil water content substitution. We should put soil volumetric water content into Formulas 3 and 4, but soil volumetric water content was replaced by soil mass water content in this study, which is less than the actual soil volumetric water content. Therefore, the calculated value of soil permittivity becomes smaller, the propagation velocity of EM wave in soil layer increases, and the estimated thickness of soil layer also increases. Figure 9 shows the correlation between the estimated thickness values of the two models and the measured thickness values in the field. The correlation coefficient is about 0.77, and the estimated value is about 1.02 times of the measured value.

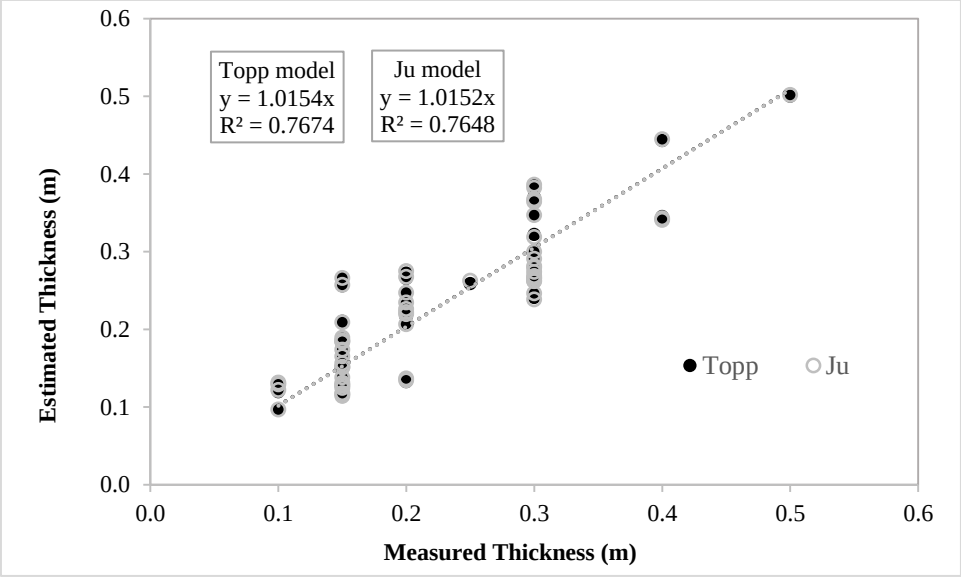

Figure 9. Correlation between estimated thickness and measured thickness of soil layers.

(2) Generally speaking, the peak or trough in the amplitude-time plots is taken as the boundary point of soil layer identification, but the occurrence of dual peaks in the spectrum of the same

soil layer would increase the error of horizon identification. Now we found three reasons for the dual peak phenomenon: first, high water and salt content lead to significant main peak and secondary peak, such as the dual peaks in 0-40cm soil layer of Spot 15 (Figure 7); second, the dense cotton planting (Figure 1) makes GPR difficult to move, which inevitably leads to the instrument leaving the ground, such as the dual peaks on the ground surface in Spot 21 (Figure 7); third, the inhomogeneous soil of the cultivation layer may lead to dual peaks phenomenon, such as the dual peaks at the bottom of 0-30cm soil layer in Spot 11 (Figure 4).

5.1.3. Reasons for the reduction of estimation error of soil layer thickness

There are two main reasons for reducing the estimation error of soil layer thickness : one is that the investigated soil is formed by river sediment deposition with little disturbance during the formation process, so the soil layers are smooth and continuous, which is conducive to radar signal recognition; the other is that we can identify soil stratigraphy more accurately by comparing the amplitude-time plot and spectrum image, and extract the two-way travel time at the soil layer interface from the amplitude-time data matrix. The average error of the estimated soil layer thickness is 0.040m, and the error of 54 soil layers in 58 soil layers is less than 0.1 m (Figure 10). When the transition between soil layers seems to be gradual and the depth of each soil layer is taken as an integer in the field (such as 15cm, 30cm, 45cm, etc.), the uncertainty of error variation is inevitable.

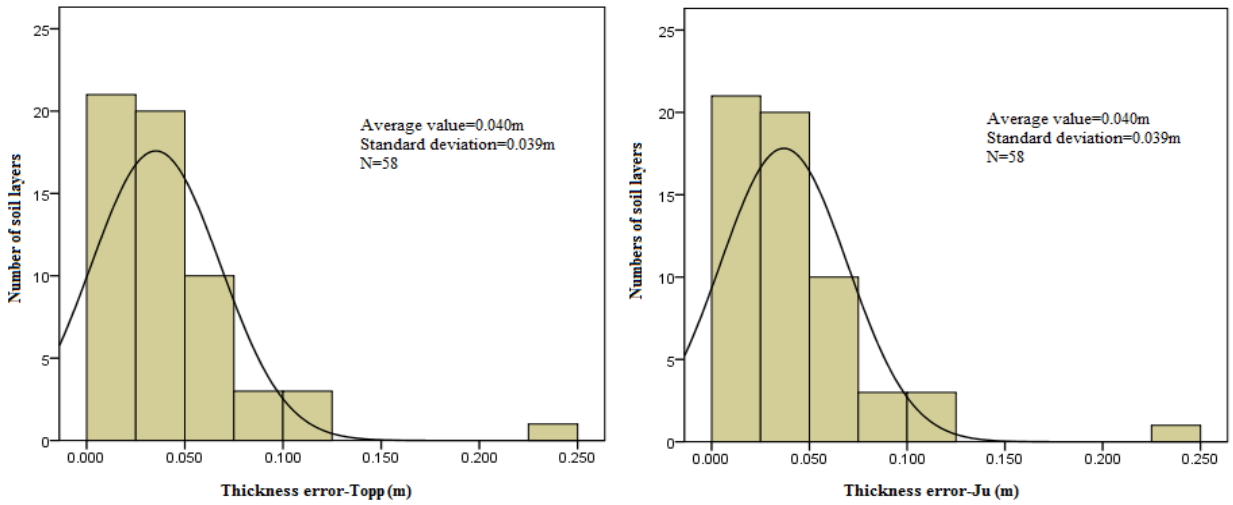

454

455 **Figure 10.** Error estimation of soil layer thickness with Topp model and Ju model.

456 **5.2. The relationship between envelope amplitude energy and soil characteristics**

457 Soil physical and chemical characteristics comprehensively affects EM wave signal and the
458 recognition of soil profile stratigraphy. At present, many research results have established the
459 relationship between EM wave amplitude energy and the dielectric permittivity, water content or
460 other characteristics of shallow stratum. Di Matteo et al. [2013] used the homogenous half-space
461 model to calculate the waveform instantaneous amplitude values averaged over different time
462 windows and found a clear inverse linear dependence with the soil surface dielectric permittivity.
463 Cui et al. [2014] used the method of Auto-Regressive and Moving Average (ARMA) power
464 spectral recognition and found the relation between power spectrum and water contents and
465 degrees of compactness of sandy loam soil. Wu et al. [2015] used the radar wave average
466 envelope amplitude (AEA) method and got the similar soil water content with TDR and drilling
467 sampling, which root mean square errors were 0.020 $cm^3 \cdot cm^{-3}$ and 0.031 $cm^3 \cdot cm^{-3}$.

468 This study also analyzed the correlation between the envelope amplitude energy value and soil
469 characteristics of each soil layer. Because the traveling velocity and time of EM wave is various
470 in each soil layer, the maximum, minimum and average value of amplitude energy cannot
471 accurately express the change rule of EM wave signal. In addition, because the attenuation form
472 of EM wave signal in each soil layer is different, the second derivative value of envelope
473 amplitude with time can reflect the influence of soil characteristics on EM wave signal better
474 than the amplitude envelope value and the first derivative value of amplitude envelope with time.
475 The second derivative value of envelope amplitude (SDEA) in each soil layer can be calculated
476 as:

477 $$\mathrm{SDEA} = \frac{d^2(\int_{t_1}^{t_2} E(t)dt)}{dt^2} \quad (8)$$

478 Where E presents the absolute value of amplitude energy (mV), t_1 and t_2 present the initiation
479 and termination time of EM wave propagation in a soil layer (ns), respectively. The extraction
480 method of traveling time is introduced in the step ③of Chapter 3.3.

481 58 soil layers were extracted from 22 spots for analysis. Through the test for two related samples
482 of nonparametric tests on SPSS software, the results of wilcoxon method and sign method were
483 consistent with P value less than 0.05, indicating that SDEA value had the same distribution with
484 soil water content, EC value, bulk density value and clay content (Table 4).

485 **Table 4.** Nonparametric test results between SDEA and each soil characteristic.

Test Method	Test Parameters	SDEA/water	SDEA/EC	SDEA/bulk density	SDEA/clay
Wilcoxon	Z	-6.616	-6.624	-6.624	-6.624

Method		P (2-tailed)	0.000	0.000	0.000	0.000
	Ranks	Negative Ranks	57	58	58	58
		Positive Ranks	1	0	0	0
Sign Method		Z	-7.222	-7.484	-7.484	-7.484
		P (2-tailed)	0.000	0.000	0.000	0.000
	Ranks	Negative Ranks	57	58	58	58
		Positive Ranks	1	0	0	0

Through the partial correlation analysis, we can find out the influence of soil characteristics on SDEA (Table 5). The significant correlation exists between SDEA and soil water content, EC value and bulk density with P value less than 0.05. The higher the soil water or salt content is, the lower the SDEA value is. The increase of soil bulk density may lead to the decrease of soil porosity and water content. The partial correlation coefficient between soil bulk density and soil water content is -0.392 with P value of 0.001. When the soil water decreased, SDEA increased. There is a positive correlation between clay content and amplitude change rate, which is different from previous research results [*Doolittle et al.*, 2007], which may be because the groundwater level in the coastal area is high, the vertical movement of soil water and salt is mainly affected by climatic factors, such as sunshine and temperature, and not closely related to the clay content. The relationship between SDEA and soil water content, EC Value and bulk density is logarithmic function, power function and linear function, respectively (Figure 11). However, the influence of soil factors on SDEA is weak and the Pearson correlation coefficients are not very high. This is mainly due to the strong interaction among soil characteristics, such as soil water content and bulk density. Alternatively, the stratified samples in the field may be more

501 inhomogeneous than laboratory-made experimental materials, so the correlation coefficients are
502 low.

503 **Table 5.** The partial correlation analysis results.

Factors	Parameters	Water	EC	Bulk density	Clay
SDEA	Pearson Correlation Coefficient	-0.393	-0.234	0.226	0.129
	Sig. (1-tailed)	0.001	0.038	0.044	0.168
	N	58	58	58	58
Water	Pearson Correlation Coefficient	-	0.197	-0.392	0.151
	Sig. (1-tailed)	-	0.069	0.001	0.129
	N	58	58	58	58
EC	Pearson Correlation Coefficient	0.197	-	0.148	0.009
	Sig. (1-tailed)	0.069	-	0.133	0.473
	N	58	58	58	58
Bulk density	Pearson Correlation Coefficient	-0.392	0.148	-	-0.017
	Sig. (1-tailed)	0.001	0.133	-	0.449
	N	58	58	58	58
Clay	Pearson Correlation Coefficient	0.151	0.009	-0.017	-
	Sig. (1-tailed)	0.129	0.473	0.449	-
	N	58	58	58	58

504

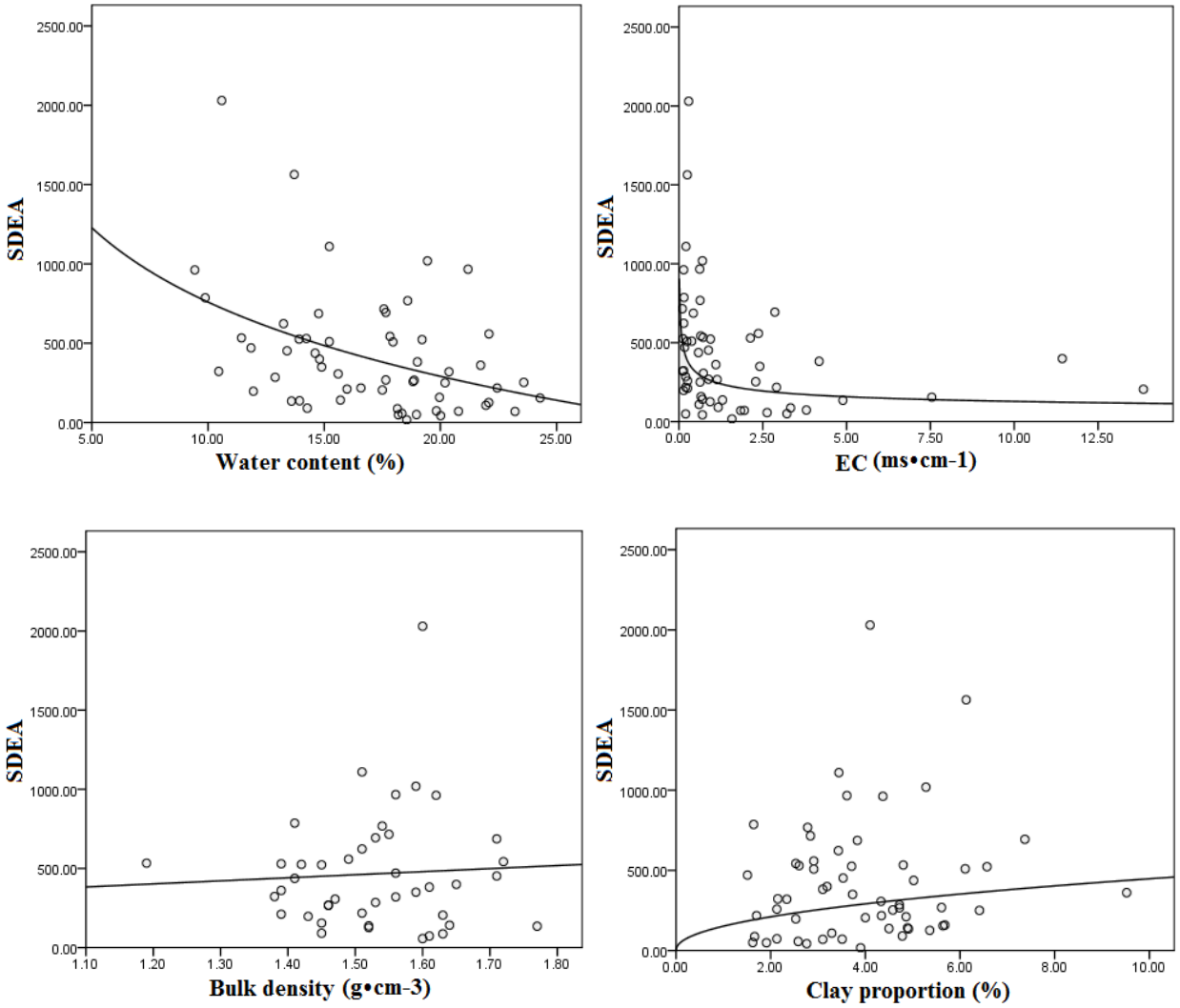

Figure 11. Curve fitting results between SDEA and soil characteristics

6. Conclusions

Through the survey of 22 typical soil profiles along 11 Yellow River tail swings in different periods, the soil dielectric permittivity and EM wave propagation velocity are calculated with measured soil water content. We acquire the time of EM wave propagation from the amplitude-time matrix, and finally calculate the thickness of each soil layer. In this study of soil profile stratigraphy determination by GPR, we found that:

514 (1) GPR can be used to identify the 0-1m soil profile stratigraphy in the saline alkali area of the
515 modern Yellow River Delta. It can identify the cultivation layer under different land use patterns.
516 The more similar the morphological characteristics of spectral images are, the closer the soil
517 properties are.

518 (2) By comparing GPR spectrum image with the amplitude-time information, we can accurately
519 identify soil stratigraphy and extract two-way travel time at soil interface, which is helpful to
520 reduce the estimation error of soil layer thickness. The average error of the estimated soil layer
521 thickness is 0.040m, which indicates the suitability of GPR for soil survey in this modern Yellow
522 River Delta.

523 (3) Soil physical and chemical characteristics comprehensively affects the EM wave signal of
524 GPR and the identification of soil profile stratigraphy. The compound effect of soil water and
525 salt is strong, and the second derivative values of envelop amplitude energy have negative
526 logarithmic function and power function with soil water content and EC values, respectively.

527 (4) GPR data processing can be simplified into three steps: filtering, zero-time adjusting and
528 gaining. This method is suitable for coastal saline land area of Yellow River Delta, and also
529 provides reference for GPR data analysis of soil profile stratigraphy in river alluvial plain area.

530 **Acknowledgment**

531 We give our thanks to X. W. Zhao, Q. C. Li, Y. F. Wang and Y. Q. Wang for soil sample
532 collection and GPR measurement. The authors would also like to thank the anonymous reviewers
533 for their constructive suggestions. This work was supported by National Natural Science
534 Foundation of China (Grant No. 41701238) and Shandong Provincial Natural Science
535 Foundation (Grant No. ZR2017BD032). The data of the Yellow River channel changes are

536 referred to the book "Soil and Environment of the Yellow River Delta" written by Yantai Coastal
537 Zone Research Institute, Chinese Academy of Sciences. All GPR measurement data and
538 experimental analysis data of soil samples applied in this paper are available from the authors
539 upon request (wpqfnu@qfnu.edu.cn).

540 **References**

541 Aranha, P.R.A., Augustin, C.H.R.R., and Sobreira, F.G.J.J.O.A.G. (2002), The use of GPR for
542 characterizing underground weathered profiles in the sub-humid tropics. *J. Appl. Geophys.*,
543 *49*(4), 195-210.

544 Brevik, E. C., Calzolari, C., Miler, B. A., Pereira, P., Kabala, C., Baumgarten, A., and Jordán, A.
545 (2016), Soil mapping, classification, and pedologic modeling: History and future directions.
546 *Geoderma*, *264*, 256-274.

547 Butnor, J.R., Campbell, J.L., Shanley, J.B. and Zarnoch, S.J. (2014), Measuring soil frost depth
548 in forest ecosystems with ground penetrating radar. *Agr. Forest Meteorol., 192*, 121-131.

549 Cao, B., Gruber, S., Zhang, T., Li, L., Peng, X., Wang, K., Zheng, L., Shao, W. and Guo H.
550 (2017), Spatial variability of active layer thickness detected by ground penetrating radar in the
551 Qilian Mountains, Western China. *J. Geophys. Res. Earth Surf., 122*, 574-591,
552 doi:10.1002/2016JF004018.

553 Cao, Q., Song, X.D., Yang, S.H., Wu, H.Y. and Zhang, G.L. (2019), Identification of plinthitic
554 red earth layers in red soil regions typical of South China with ground penetration radar. *Acta*
555 *Pedological Sinica, 56*(4), 813–824.

556 Casey, D.K., Sophie, W., Maggie, P., Anthony, R. B., Peter, J.A.K. and Ray B.B. (2018), A
557 geospatial model to quantify mean thickness of peat in cranberry bogs. *Geoderma, 319,* 122-
558 131.

559 Cavallo, G., De Benedetto, D., Castrignanò, A., Quarto, R., Vonella, A.V. and Buttafuoco, G.
560 (2016), Use of geophysical data for assessing 3D soil variation in a durum wheat field and
561 their association with crop yield. *Biosyst. Eng., 152,* 28-40.

562 Cui, F., Liu, J., Wu, Z., Guo, Z. and Wu, Y. (2014), Application of ground penetrating radar
563 power spectrum model in detection of water content and degrees of compactness in sandy
564 loam. *Trans. of the CSAE, 30*(16), 99-105.

565 Davis, J.L.& Annan, A.P. (1989), Ground-penetrating radar for high-resolution mapping of soil
566 and rock stratigraphy. *Geophys. Prospect, 37*(5), 531-551.

567 Di Matteo, A., Pettinelli, E. and Slob, E. (2013), Early-Time GPR Signal Attributes to Estimate
568 Soil Dielectric Permittivity: A Theoretical Study. *IEEE T. Geosci. Remote, 51*(3), 1643-1654.

569 Dobson, M.C., Ulaby, F.T., Hallikainen, M.T. and El-Rayes, M.A. (1985), Microwave dielectric
570 behavior of wet soil-Part II: Dielectric mixing models. *IEEE T. Geosci. Remote, 1,* 35-46.

571 Doolittle, J.A., Minzenmayer, F.E., Waltman, S.W., Benham, E.C., Tuttle, J.W. and Peaslee,
572 S.D. (2007), Ground-penetrating radar soil suitability map of the conterminous United States.
573 *Geoderma, 141*(3-4), 416-421.

574 Gan, Y.D., Huang, X.M., Li, S.S., Liu, N., Li, Y.C.C., Ariel F., Wang, W.X., Wang, R.Q. and
575 Dai, J.L. (2019), Source quantification and potential risk of mercury, cadmium, arsenic, lead,
576 and chromium in farmland soils for Yellow River Delta. *J. Clean. Prod., 221,* 98-107.

577 Hnninen, P. (1992), Application of ground penetrating radar techniques to peatland
578 investigations. Proc. 4th Int. Conf. GPR, Rovaniemi, Finland, 217–221.

579 Hu, Z.Q., Chen, X.T., Lu, X., Xu, H.F. and Zhang, J. (2006), Microwave spectrum analysis of
580 salinity pollution about reclamation soil. *Trans. of the CSAE, 22*(6), 56–60.

581 Inman, D.J., Freeland, R.S., Yoder, R.E., Ammons, J.T. and Leonard, L.L.J.S.S. (2001),
582 Evaluating GPR and EMI for morphological studies of loessial soils. *Soil Sci., 166*(9), 622-
583 630.

584 Jackson, T.J., Schmugge, J. and Engman, E.T. (1996), Remote sensing applications to
585 hydrology: soil moisture. *Hydrolog. Sci. J., 41*, 517-530.

586 Ju, Z.Q. (2005), Dielectric permittivity and its relationship with water content for several soils in
587 China. M.S. dissertation, Coll. Res. Environ., China Agr. Univ., Beijing, China.

588 Kumar, V.S., Dhakate, R., Amarender, B. and Sankaran, S. (2016), Application of ERT and GPR
589 for demarcating the saline water intrusion in coastal aquifers of Southern India. *Environ.*
590 *Earth Sci., 75*(5), 393.

591 Lei, L., Tashpolat, T., Ding, J.L., Jiang, H.N., Yao, Y., Sun, Y.M., Xia, J. and Ardak, K. (2013),
592 Constant characteristic and model verification of saline soil dielectric in arid area. *Trans. of*
593 *the CSAE, 29*(16), 125-133.

594 Li, X.J., Hu, Z.Q., Li, S.C. and Cai, Y.F. (2015), Anomalies of mountainous mining paddy in
595 western China. *Soil Till. Res., 145*, 10-19.

596 Liu, J.K., Bernard, A.E., Dai, L.Y., Wang, Y., Wu, Y.N., Yan, G.X., Cong, L., Zhai, J.X., Zhang,
597 Z.M. and Zhang, M.X. (2019), Capturing hydrological connectivity stratigraphy of wetlands
598 with indices based on graph theory: A case study in Yellow River Delta. *J. Clean. Prod.*, *239*,
599 1-8.

600 Lombardi, F. & Lualdi, M.J.R.S. (2019), Step-Frequency Ground Penetrating Radar for
601 Agricultural Soil Morphology Characterisation. *Remote Sens-Basel*, *11*(9), 1075.

602 Loulizi, A. (2002), Development of ground penetrating radar signal modeling and
603 implementation for transportation infrastratigraphy assessment. Ph.D. dissertation, Dept. Civ.
604 Environ. Eng., Virginia Tech., Blascksburg, VT, USA.

605 Luo, G.B., Cao, Y.G., Bai, Z.K., Huang, Y.H. and Wang, S.F. (2019), Soil bulk density
606 difference, ground penetrating radar feature identification, and simulation for a reclaimed soil
607 profile in the dumping site of an open pit mine. *JARE*, *36*(4), 441-452.

608 Maury, S. & Balaji, S. (2015), Application of resistivity and GPR techniques for the
609 characterization of the coastal litho-stratigraphy and aquifer vulnerability due to seawater
610 intrusion. *Estuar. Coast. Shelf S.*, *165*, 104-116.

611 Peng, L., Zhang, L. and Deng, Y. (2009), Study on salt migration in saline soil using GPR. Proc.
612 8th Int. Symp. Permafrost Eng., Xi'an, China, 698–707.

613 Romero-Ruiz, A., Linde, N., Keller, T. and Or, D. (2018), A Review of Geophysical Methods for
614 Soil Stratigraphy Characterization. *Rev. Geophys.*, *56*(4), 672-697.

615 Samson, C., Mah, J., Haltigin, T., Holladay, S., Ralchenko, M., Pollard, W. and Monteiro Santos,
616 F.A. (2017), Combined electromagnetic geophysical mapping at Arctic perennial saline

springs: Possible applications for the detection of water in the shallow subsurface of Mars. *Adv. Space. Res.*, *59*(9), 2325-2334.

Sass, O., Friedmann, A., Haselwanter, G. and Wetzel, K.-F. (2010), Investigating thickness and internal structure of alpine mires using conventional and geophysical techniques. *Catena*, *80*, 195-203.

Scudiero, E., Berti, A., Teatini, P. and Morari, F. (2012), Simultaneous Monitoring of Soil Water Content and Salinity with a Low-Cost Capacitance-Resistance Probe. *Sensors*, *12*(12), 17588-17607.

Sukhobok, Y.A., Pupatenko, V.V., Stoyanovich, G.M. and Ponomarchuk, Y.V.J.P.E. (2016), Soil formation lithological profiling using ground penetrating radar. *Procedia Engineering*, *143*, 1236-1243.

Topp, G.C., Davis, J. and Annan, A.P. (1980), Electromagnetic determination of soil water content: Measurements in coaxial transmission lines. *Water Resour. Res.*, *16*(3), 574-582.

Truman, C., Perkins, H., Asmussen, L., Allison, H.J.J.O.O. and Conservation, W. (1988), Using ground-penetrating radar to investigate variability in selected soil properties. *J. Soil. Water Conserv.*, *43*(4), 341-345.

Walter, J., Hamann, G., Luck, E., Klingenfuss, C. and Zeitz, J. (2016), Stratigraphy and soil properties of fens: Geophysical case studies from northeastern Germany. *Catena*, *142*, 112-125.

Wang, P., Hu, Z., Zhao, Y. and Li, X. (2016a), Experimental study of soil compaction effects on GPR signals. *J. Appl. Geophys.*, *126*, 128-137.

638 Wang, P., Li, X.J., Min, X.Y., Yang, D., Wang, X., Li, J.Y. and Sun, X.Y. (2016b),
639 Experimental study on GPR measurement of coastal saline soil profile. *Soils, 48*(6), 1261-
640 1269.

641 Wang, P., Li, X.J., Sun, X.Y., Liu, F., Min, X.Y. and Yang, D. (2017), Determination of water
642 content of coastal saline top soil with GPR. *Chinese J. Soil Sci., 48*(6), 1329-1337.

643 Wang, S., Chen, H.S., Fu Z.Y., Nie, Y.P. and Wang. K.L. (2016c), Estimation of thickness of
644 soil layer on typical Karst hillslopes using a ground penetrating radar. *Acta Pedological*
645 *Sinica, 36*(1), 129-135.

646 Wang, T.P., Chen, C.C., Tong, L.T., Chang, P.Y., Chen, Y.C., Dong, T.H., Liu, H.C., Lin, C.P.,
647 Yang, K.H., Ho, C.J. and Cheng, S.N. (2015), Applying FDEM, ERT and GPR at a site with
648 soil contamination: A case study. *J. Appl. Geophys., 121*, 21-30.

649 Widess, M.B. (1973), How thin is a thin bed. *Geophys., 38*, 1176-1180.

650 Wu, Z., Peng, S., Du, W. and Cui, F. (2015), Detection of soil water content using ground
651 penetrating radar average envelope amplitude method. *Trans. of the CSAE, 31*(12), 158-164.

652 Xue, J., Zeng, Z.F., Tian, G. and Wang, Z.J. (2006), The application of GPR to detecting the
653 saline-alkali layer in west Jilin. *Geophys. Geochem. Explor., 29*(5), 421-424.

654 Yao, R.J., Yang, J.S. and Liu, G.M. (2006), Spatial variability of soil bulk density in the Yellow
655 River Delta. *J Irrig. Drain., 25*(4),11-15.

656 Yao, R.J. & Yao, J.S. (2007), Quantitative analysis of spatial distribution pattern of soil salt
657 accumulation in plough layer and shallow groundwater in the Yellow River Delta. *Trans. of*

658 *the CSAE, 23*(8), 45-51.

659 Zajícová, K. & Chuman, T. (2019), Application of ground penetrating radar methods in soil
660 studies: A review. *Geoderma, 343*, 116-129.

661 Zhang, J., Lin, H. and Doolittle, J. (2014), Soil layering and preferential flow impacts on
662 seasonal changes of GPR signals in two contrasting soils. *Geoderma, 213*, 560-569.

663 Zhang, M.X. (2010), Dynamic prediction and regulation of soil water and salt. Science Press,
664 Beijing, 13